Journal of
Materials Chemistry A

Materials for energy and sustainability

Accepted Manuscript

This article can be cited before page numbers have been issued, to do this please use: P. Richtr, D. Gráf, M. Drnec, J. Charvát, M. Bureš, O. Navrátil, J. Pocedi, J. Kosek and P. Mazur, *J. Mater. Chem. A*, 2026, DOI: 10.1039/D5TA07792C.

ROYAL SOCIETY OF CHEMISTRY

rsc.li/materials-a

View Article Online
DOI: 10.1039/D5TA07792C

Understanding the degradation process in zinc-iodine hybrid flow batteries

Přemysl Richtr[a], David Gráf[a], Martin Drnec[a], Jiří Charvát[b, c], Martin Bureš[a], Ondřej Navrátil[a], Jaromír Pocedič[b, c], Juraj Kosek[a, c], Petr Mazúr[a, c]

[a]University of Chemistry and Technology Prague, Department of Chemical Engineering, Technicka 5, 166 28 Prague, Czech Republic
[b]Pinflow energy storage, s.r.o., Křižovnická 86/6, 110 00 Prague, Czech Republic
[c]New Technologies – Research Centre, University of West Bohemia, Univerzitní 8, 306 14, Plzeň, Czech Republic

Abstract

Zinc-iodine hybrid flow battery (ZIHFB) represents a promising stationary energy storage with a theoretically high volumetric capacity (>250 Ah L^{-1}), however, its broader commercialization is obstructed mainly by its reduced lifetime, particularly when charging to a higher areal capacity of the negative half-cell (>130 mAh cm^{-2}). In our study, we investigated the origins of the performance degradation of a lab-scale ZIHFB single-cell due to excessive charging. It has manifested as a local peak on the charging voltage profile (voltaic bulge), resulting in decreased coulombic efficiency on the subsequent battery cycling. Systematic variation of the selected experimental conditions (incl. charging SoC limit, electrolyte composition) and battery construction (use of non-conductive felt in individual half-cells, hydraulic shunt of electrolyte tanks), together with *post mortem* characterization of the inner cell components (pressurized membrane tightness test, microtomographic evaluation of Zn distribution within the felt electrodes), revealed the origin of performance degradation. It originates from a non-homogeneous Zn deposition leading to a formation of a compact zinc layer near the electrode-membrane interface, which restricts ionic supply to the rest of 3D negative electrode. As a consequence, Zn dendrites growth towards the positive electrode is promoted, leading to membrane perforation and its malfunction. With the optimized operating conditions and battery construction, we achieved stable and efficient mid-term cycling with coulombic efficiency ≥ 95% and energy efficiency > 83% at 100 mA cm^{-2}, and a low-capacity fade of 0.02% per cycle. The deepened insight into the degradation mechanism will be further used to design effective mitigation strategies to enhance the areal capacity and durability of ZIHFBs and related zinc-based chemistries.

1. Introduction

Stabilization of the electricity grid is the compulsory step achieve the full potential of renewable energy sources. The most widely spread types of energy storage (ES) are physical-based and electrochemical-based ones. [1, 2] Pumped hydro energy storage (PHES), compressed air, and flywheel technologies are the representatives of physical-based ES, with PHES being the most dominant among the technologies, despite low flexibility, limited availability of suitable sites, and high-investment costs. Li-ion batteries are the most dominant electrochemical ES technologies due to their high efficiency and energy density. Nonetheless, the high risk of fire and growing demand for the battery in e-mobility motivate R&D of alternative systems, incl. redox flow batteries

View Article Online
DOI: 10.1039/D5TA07792C

(RFBs). The main advantages of RFBs are safety (non-flammability due to the use of aqueous electrolytes) and flexible scalability (decoupled power and capacity). [3, 4] So far, the vanadium redox flow battery (VRFB) represents the most developed system, which excels in long life-time (up to 15 000 cycles, 20 years), easy recyclability, and residual cost of electrolytes. However, high capital expenditures (CAPEX) due to high vanadium price, and low energy density hinder their commercialization. [5-10]

As an alternative, hybrid flow batteries (HBFs) with metal deposition are being developed due to their theoretically higher energy density and abundant resources of metals such as zinc or iron. In this concept, a metal is being deposited on the negative electrode during battery charging, while it is being dissolved during discharging. The battery capacity is thus given by two factors: the concentration of active species dissolved in the electrolytes (volumetric capacity), and by the molar amount of metal which can be reversibly deposited within the negative half-cell (areal capacity, Q_{areal}).

Various HFB chemistries have been reported. All-iron HFB excels in cost effectiveness of the active materials, low environmental impact, and high safety. On the other hand, a low redox potential of iron deposition promotes a parasitic hydrogen evolution reaction (HER) on the negative electrode at a relatively high rate, which is responsible for decreased coulombic efficiency and a loss of capacity as a result of faradaic imbalance between the electrolytes. Thus, an additional recombination cell is typically needed which increases the complexity of storage. [11]

Zinc is another popular metal often used in HFBs, with various posolyte chemistries incl. zinc-air hybrid flow battery (ZAHFB), zinc-bromine hybrid flow battery (ZBHFB), or zinc-iodine hybrid flow battery (ZIHFB). Similar to Fe-based systems, zinc-based HFB suffers from non-homogeneous metal deposition and dendrite formation, Zn corrosion, and side reactions such as hydrogen evolution which negatively influence the efficiency and stability of those batteries. [12] While ZBHFB has the highest nominal OCV (1.85 V), a relatively low cost of active species, and high energy efficiency (*EE*), its applicability is limited due to the toxicity and high volatility of Br_2. ZAHFB has a slightly lower nominal OCV (1.65 V) and the use of ambient air on the positive electrode make these batteries non-toxic and cost effective in terms of capacity. However, poor efficiency and stability of positive electrode reactions, together with the need for expensive electrocatalysis, obstruct the commercialization of these batteries. ZIHFB has the lowest nominal OCV of 1.3 V, which is, however, compensated by high volumetric capacity (ZnI_2 solubility goes up to 5 mol dm^{-3}) with a theoretical energy density of 167 Wh dm^{-3}. In addition, the redox kinetics of the iodine active species reaction on cheap carbon-based electrodes is faster compared to those of other halogen elements such as chlorine or bromine. [13] The electrode reactions, including their standard redox potentials, are stated below (see **equations 1-4**):

$$Zn^{2+} + 2\,e^- \rightleftharpoons Zn^0 \qquad E^\circ = -0.763 \text{ vs. NHE} \qquad (1)$$

$$2\,I^- \rightleftharpoons I_2 + 2\,e^- \qquad (2)$$

$$I_2 + I^- \rightleftharpoons I_3^- \qquad (3)$$

$$3\,I^- \rightleftharpoons I_3^- + 2\,e^- \qquad E^\circ = 0.534 \text{ vs. NHE} \qquad (4)$$

View Article Online
DOI: 10.1039/D5TA07792C

During the charging, zinc is being deposited from solution (according to **equation 1**) and therefore Zn^{2+} concentration decreases in the negative electrolyte, while the reaction proceeds in the opposite direction during the battery discharge. In the positive half-cell, I^- is being oxidized to low-soluble I_2 during the charging (see **equation 2**) which consequently complexes with excess I^- to form highly soluble I_3^- (see **equation 3**). Thus, only two thirds of the iodine in the electrolyte is used for the energy storage [13]. At higher states of charge (SoC), higher order polyiodides can also be formed which makes the posolyte chemistry relatively complex. Jang et al. [14] reported that during charging, a compact temporary film of adsorbed I_2 can be formed on the surface of the positive electrode, which significantly increases charge transfer resistance of the battery. This explains the observed increase in cell overpotential by more than 300 mV when charging at high current densities (>400 mA cm^{-2}). The mentioned phenomenon can significantly limit the maximal operating power densities. In addition, I_3^- has a strong oxidizing strength, which enables fast dissolution of metallic zinc (self-discharge), according to **equation 5**:

$$Zn^0 + I_3^- \rightarrow 3\ I^- + Zn^{2+} \quad (5)$$

Negative half-cell is linked with common limitations of zinc-based HFBs, such as poor cyclability, non-homogeneous zinc deposition (incl. dendrite formation), zinc oxidation, and passivation by a precipitated layer of zinc oxide or parasitic HER. [15-17] These challenges can be addressed differently, e.g., by optimizing hydrodynamic conditions of the flowing electrolyte [18], application of proprietary charging protocols (e.g., pulse charging) [19], or by applying electrolyte additives. [20, 21] $Q_{areal,}$ i.e., the amount of Zn that can be safely stored in a battery is influenced (in addition to the negative half-cell geometry) by the morphology of the deposited zinc which can occur in three different morphologies: mossy (porous), crystalline (compact), and dendritic (needle-like). [17, 22] Obviously, crystalline morphology is preferable due to the highest density and the best adhesion to the electrode substrate. The nature of morphology is known to be strongly dependent on the operating conditions (current density, electrolyte flow rate, bulk reactant concentration), affecting the thickness of the diffusion layer close to the electrode-electrolyte interface. According to Dundálek et al. [15], morphology can be predicted by the so-called current density ratio, CDR, i.e. ratio of actual current density to the limiting one. Although low CDRs provide mossy structures, deposition close to limiting current densities promotes dendrite formation. It is worth to mention that a limiting current strongly depends on reactant concentration, local flow velocities, and temperature, thus optimal CDR can significantly vary during the cycling.

For deposition planar substrate electrodes can be used, however, due to the limited mass transfer of the reactants (Zn^{2+}) to the electrode surface, 3D electrodes are used more often. The 3D electrode can be either metallic [23] or carbon-based [21, 24, 25], the latter one being a common material in RFBs, typically in the form of a non-woven felt of graphitized polymeric fibres (graphite felt, GF). The 3D structure of GF increases the surface area available for the reaction, thus decreasing local current densities. However, with the GF electrode, it can be expected that the deposited zinc is preferentially localized closer to the membrane/separator, compared to the planar electrode, due to higher (by one or two orders of magnitude) electronic conductivity of GF when compared to the ionic conductivity of the electrolyte. [21] Deposition of zinc closer to the membrane/separator can lead to faster penetration of zinc dendrites through the membrane, causing a cell performance degradation due to the electric shortcut.

View Article Online
DOI: 10.1039/D5TA07792C

The choice of a suitable electrode separator is a very important parameter in the design of a flow battery cell/stack. [26] The separator is responsible for the mutual electronic separation of the negative and positive half-cells (preventing internal short-circuit), while it enables their ionic interconnection. In most RFB systems, it also prevents mutual cross-contamination of the electrolytes. In principle, both porous separators and ion-exchange membranes (IEMs) can be used in ZIHFB. The porous separator, typically a thin polymeric film with small pores (units to tens of μm), significantly reduces a convective flux of the electrolytes between the individual half-cells, while enabling fast ionic transport for charge equalization during the battery operation. However, compared to IEMs, its perm-selectivity is much lower, which results in lower coulombic efficiency (*CE*) and faster capacity fade of battery operation due to active species cross-over. The lower ion selectivity of porous separators is compensated by typically a much lower price and better mechanical and chemical stability over a long operation time. The ionic conductivity of the separator soaked in a given electrolyte is mainly given by the pore structures, thickness. [27]

IEMs are typically ion-selective polymeric separators with immobilized ionic functional groups in their structure and pore size in units of nm which yields in a preferential transport of either anions (in case of anion-exchange membranes (AEMs)) or cations (for cation-exchange membranes (CEMs)). Battery performance can be optimized by tuning the membrane properties such as polarity of functional groups and their concentration (ion-exchange capacity, IEC), chemical composition of the polymer (e.g., length of side-chains) or its thickness. Thinner membranes with high IEC are generally more suitable for efficient battery operation at high current densities, enabling fast ionic transport but lower selectivity. [13, 26, 28]

In ZIHFB, the primary use of CEMs has been reported, mostly Nafion by Chemours Company, as recently reviewed by Fan, D., et al.. [13] With CEMs, the supporting electrolyte cations, as well as the Zn^{2+} ions can cross-over the membrane during battery operation. The concentration of Zn^{2+} ions in the negolyte decreases significantly during the battery operation due to their conversion to metallic Zn (see **Figure 2**). Thus, in the case of miscible electrolytes (i.e., with an initial equal composition of both electrolytes), Zn^{2+} can permeate from posolyte due to the concentration gradient. As the permselectivity of IEMs is never ideal, particularly in such highly concentrated electrolytes, minor permeation of iodide ions to posolyte and tri-iodide ions to negolyte can also take place, resulting in reduced *CE* due to Zn oxidation (self-discharging by tri-iodides, according to **eq. 5**).

The properties of the separator used can significantly affect the battery performance and lifetime, particularly the issues related to the internal short circuit caused by the growth of the zinc dendrites during battery charging, which is a common problem for zinc-based batteries. In general, larger pores of porous separators, when compared to IEMs, should simplify these degradation phenomena. Interestingly, Xie et al. [29] reported the use of a polyolefin-based separator with high ion conductivity, showing a stable ZIHFB operation due to the so-called self-healing effect. This effect can be described as a self-discharge reaction of I_3^- with zinc dendrites that have grown into the pores of the separator which results in the continuous dendrite dissolution (according to **eq. 5**) without deterioration of the battery performance, just for the price of lower *CE*. To further improve ZIHFB, Xie et al. [30] manufactured a composite membrane by applying a thin layer of Nafion

View Article Online
DOI: 10.1039/D5TA07792C

polymer on the previously used polyolefin porous separator to enhance the perm-selectivity of the separator. Due to the application of a thin Nafion layer, the *CE* was increased by 11%, when compared to the cell with pristine separator, due to reduced I_3^- cross-over from posolyte. The single-cell with the composite membrane showed stable performance at 80 mA cm^{-2} for 500 cycles without any efficiency or capacity decay.

Kellamis et al. [21] demonstrated enhanced battery performance thanks to the use of gluconate electrolyte additive together with the use of a non-conductive polymeric felt (NCF) on each side of the battery cell. The use of NCF in the negative half-cell and the addition of NCF to the positive one (combination of conductive GF and NCF on positive side) together with the implementation of the electrolyte additive led to the increased Q_{areal} from 60 mAh cm^{-2} (obtained with a standard flow battery construction) to 350 mAh cm^{-2} (at the beginning of the experiment, after 4 cycles the capacity was 280 mAh cm^{-2}) at current density of 100 mA cm^{-2}, with 53% voltaic efficiency (*VE*). Addition of potassium gluconate prevented the dendrite formation but also decreased the ionic conductivity of the electrolyte, which resulted in the decreased *VE*. More importantly, the presence of NCF in the positive half-cell prevented the formation of electric shorts caused by Zn dendrites. The battery of the same construction, but without the additive, achieved the initial Q_{areal} of 480 mAh cm^{-2}, however, after 8 cycles it dropped to 370 mAh cm^{-2}. Omission of the additive resulted in an increase of *VE* by approximately 8% under the given conditions. The authors demonstrated a significant increase in available Q_{areal} for ZIHFB at a reasonable current density of 100 mA cm^{-2}, that allows a significant decrease in battery stack price.

ZIHFB shows great potential for highly effective and energetically dense stationary storage, and several recent publications have shown a potential for successful scale-up. However, commercialization of current ZIHFBs is still limited by low Q_{areal} of the negative battery half-cell. [21] When the critical amount of Zn is deposited, battery charging overvoltage gradually increases, which is eventually followed by its sudden drop upon further charging. This behaviour, manifested as a "voltaic bulge" on the charging voltage profile, leads to irreversible battery performance degradation, and it has been, to some extent, already reported in the literature [21, 31], however, without adequate effort for a deeper understanding of the phenomena origins and mechanisms. In most cases, its presence is simply avoided thanks to sufficiently low charging voltage or capacity limit. The problem has been briefly reported by Kellamis et al. [21], stating that the increased charging overvoltage is mostly related to increased mass transfer polarization, while the subsequent overvoltage drop is directly linked to the internal short-circuit of the battery by the deposited Zn. However, to the best of our knowledge, a sufficiently detailed description of the voltaic bulge phenomenon, its origins, and exact degradation mechanism is still missing, which complicates the design of effective measures for enhancing battery performance at increased Q_{areal}.

In our study, we provide closer insight into the voltaic bulge phenomena thanks to a complex and systematic study based on lab-scale single-cell experiments together with *post-mortem* analysis of the battery components, which enabled us to identify origins of the observed performance deterioration at increased Q_{areal} and to propose a realistic degradation mechanism and rational mitigation measures for performance and stability enhancement. Our study is divided into three parts describing: i) identification of individual degradation phenomena, ii) evaluation methods for

View Article Online
DOI: 10.1039/D5TA07792C

recovery of the battery performance and mitigation of the degradation process, and iii) optimization of battery construction and operation to achieve stable and efficient mid-term battery performance, achieving *CE* > 96% and *VE* > 87%, at 100 mA cm^{-2} for 70 cycles with negligible capacity decay (0.02% per cycle).

2. Experimental

2.1 Construction of the flow cell and general condition

ZIHFB characterization was conducted using a single-cell (construction derived from a std. lab-cell by Pinflow energy storage, s.r.o.). The single-cell design (see **Figure S1a**) was adjusted for the needs of ZIHFB (i.e., modification of the flow field design) in cooperation with Pinflow. It consists of aluminium end plates, copper current collectors, composite carbon-polymer plates, graphite felts (GFs, rayon-based), elastomeric polyolefin-based flat gaskets, electrolyte distribution frames made of PVC, and activated CEM. GF was activated according to Mazúr et al. [32] and the compression ratio (*CR*) was set to 25%. The geometric area of the electrodes was 20 cm^2 (4 x 5 cm^2). Flow-through distribution of electrolyte was used for both half-cell compartments.

The standard apparatus (see **Figure S1b**) for the characterization under ZIHFB consists of a peristaltic pump (Watson–Marlow 323), two separate electrolyte tanks, and PTFE tubing that connects the tanks to the cell. In the standard characterization negolyte tank contained 0.07 dm^3 and the posolyte 0.08 dm^3 of an electrolyte solution composed of 1 mol dm^{-3} ZnI_2, 4 mol dm^{-3} KI and 1.5 mol dm^{-3} KCl. In some experiments, different volumes of electrolytes with the same composition were used, which is clearly marked in a corresponding experiment. In other, the posolyte was used without Zn^{2+} ions, so the composition was following: 4 mol dm^{-3} KI and 1.5 mol dm^{-3} KCl. The flow rate of both electrolytes was set at 0.08 dm^3 min^{-1}. The entire testing apparatus was placed in a temperature-insulated box maintained at a given temperature of 40 °C.

2.1.1 Construction modifications of ZIHFB

To investigate the mechanism of irreversible battery performance deterioration, two different strategies were tested: i) a hydraulic connection between the electrolyte tanks (short hydraulic shunt, HS, by thin capillary positioned on bottom of both tanks), to maintain the same levels of both electrolytes during the experiment; ii) a combination of electronically conductive GF and NCF (polymeric non-conductive felt, FINET PES 1 mm, MITOP) in each half-cell (see **Figure S2**).

2.2 Electrochemical characterization of ZIHFB

For the characterization of the ZIHFB single-cell we used a complex procedure consisting of electrochemical impedance spectroscopy (EIS) and galvanostatic charge-discharge cycling combined with constant voltage discharge using the battery cycler BSC-815 (Biologic). In the monitoring apparatus Tevomet TV16 multichannel voltage monitor was added (Kolibrik.net), which enabled on-line monitoring of potentials and pressure drop measurements. Each characterization procedure was slightly different; thus, we will divide this chapter into more sub-chapters.

View Article Online
DOI: 10.1039/D5TA07792C

2.2.1 Standard ZIHFB characterization

Firstly, ZIHFB was cycled in SoC range 0-20% (SoC of negolyte), several cycles were performed, consequently SoC range was increased by 20% (i.e., 0-40% SoC range), this was repeated with stepwise increasing of charging SoC range by 20% in each step till battery was cycled in range 0-80% of the theoretical capacity of the 0.07 dm^3 of negolyte. In this article, we will refer to SoC as the ratio of the current charged capacity to the theoretical capacity of the negolyte which corresponds to the total amount of Zn^{2+} ions. Battery was always charged galvanostaticaly (CC) at a current density of 100 mA cm^{-2} to a chosen SoC limit and back-discharged in a combined galvanostatic-potentiostatic (CC-CV) mode with 0.1 V discharging voltage limit till the discharged current decreased below 10% of the charging current. Subsequently, several dozen cycles were performed with the charging SoC limit of 80%. From the charge-discharge cycling the efficiencies (*CE*, *VE,* and *EE*) and capacity utilization (*CU*) were evaluated according to std. relations [32] together with their mean values from each SoC range. *CU* was calculated with respect to the theoretical capacity of the negolyte according to Faraday´s law.

2.2.2 Detailed ZIHFB characterization

Detailed battery characterization was preformed using two different modes of EIS measurement. In the first case, the battery was gradually charged in steps with varying capacities (around area of interest, the capacity of the step was 1.5 mAh cm^{-2}) and between each step, EIS at OCV (further referred to as $PEIS_{OCV}$) was measured in a potentio mode, with a frequency ranging from 10 kHz to 25 mHz with a sinus amplitude of the perturbing signal of 20 mV. This was done using the BSC-815 battery cycler (Biologic). In the second case, EIS was measured under a constant current density load (100 mA cm^{-2}) in a galvano mode (marked $GEIS_{LOAD}$) in the frequency range from 100 kHz to 50 mHz with a multi-sine regime and the amplitude of the perturbing signal of 12.5 mA cm^{-2}. This was done with a potentiostat VSP-3e (Biologic) enabling measurements in a broader frequency range. Since the EIS was measured under current load, the battery was continuously charged (or discharged) during the impedance measurement.

From the EIS experiments, the values of area specific resistances (*ASRs*) were evaluated; the ohmic *ASR* (ASR_{Ω}) and charge transfer *ASR* (ASR_{CT}) by fitting the EIS spectra to a suitable equivalent circuit model (for equivalent circuit, see **Figure S3a**). All EIS spectra are presented as the Nyquist plot, with the direction of frequency indicated from high frequency closer to the y-axis toward low frequency toward the right (see **Figure S3b**).

2.2.3 Strategies for capacity regeneration and stable operation of ZIHFB

The rest of the experiments consisted of the electrochemical characterization techniques mentioned above. Volumes of electrolytes can differ, or some construction modifications were realized (i.e., HS of electrolyte tanks or implementation of NCF into the cell), which has been described in the **Section 2.1.1**.

Electrolyte remix

Capacity regeneration in RFB can be done by the electrolyte mixing procedure (so called electrolyte remix) to restore the initial electrolyte composition. Electrolyte remix was performed after the ZIHFB was fully discharged (i.e., after combined CC-CV discharge with potentiostatic retention at 0.1 V). Subsequently, the outlet tubes connecting the individual half-cells to the

View Article Online
DOI: 10.1039/D5TA07792C

respective electrolyte reservoirs were interchanged, and in this arrangement, the electrolytes were intensively mixed (30 min) in order to achieve full equalization of their composition and possible additional complete dissolution of zinc residues in the negative half-cell by their reaction with tri-iodide ion residues contained in the posolyte. Subsequently, the outlet tubes were reconnected to the respective reservoirs, and the electrolytes were distributed in the equal volume ratio to the respective reservoirs.

Stable electrochemical operation conditions

A cycling protocol with 10 CC cycles followed by two CC (charging) and combined CC–CV (discharging) formatting cycles (CV cut-off voltage 0.1 V until discharge current <10% of charge current) was deployed, ensuring full discharge of the negative half-cell and complete zinc dissolution. To secure safe operating conditions during the mid-term cycling stability, the charging limit was limited to 50% (negolyte volume 0.06 dm^3, Q_{areal} of 80 mAh cm^{-2}), i.e., safely below the critical capacity. Charging was terminated either upon reaching this capacity or a cell voltage of 1.55 V.

2.3 Microstructure analysis of negative electrodes

Confocal optical observations were performed using a laser scanning confocal microscope (LSCM, Keyence VK-X3000). Although the instrument is equipped with a 404 nm semiconductor laser, all images in this study were acquired using the integrated white-light LED illumination source. Depending on the region of interest, imaging parameters were adjusted as follows: a 2.5× objective lens (NA = 0.075) with an optical zoom of 0.7 and a pitch of 40.00 µm, or a 20× objective lens (NA = 0.46) with an optical zoom of 1.0 and a pitch of 0.84 µm. All measurements were performed at a brightness setting of 82.

The microstructure of the selected GF with deposited zinc was studied by micro-computed tomography (µCT, sample size 50 x 40 x 5.5 mm). The samples were scanned using an X-ray microtomograph, CT portable 160.90 (Fraunhofer). An accelerating voltage of 90 kV was used for the scanning, and 3500 images were taken for each scan with a resolution of 22.19 microns/pixel and an exposure time of 450 ms/image. The total scanning time was five hours per sample. The resulting structure was obtained from the captured images by mathematical reconstruction in the native microtomograph software.

To evaluate porosity changes in the negative electrode using µCT data, the original TIFF scans were first processed by rescaling the intensity values in a range of 0 to 1. These values were then normalized using a power-law transformation, specifically by taking the fourth root of the intensity, which helped to enhance the contrast and reduce the influence of extreme values. The resulting intensity values were further normalized so that their sum equalled one, ensuring proportional distribution across the volume.

To estimate the amount of zinc deposited in the electrode, the experimental capacity was converted to mass using Faraday's law (assuming 100% current yield) and then to the molar mass of zinc. The volume of deposited zinc was calculated by dividing this theoretical Zn mass by the density of metallic zinc and correcting it for effective zinc density, assumed to be 0.7 (of metallic zinc) based on the literature. [33] This total zinc volume was then distributed throughout the 3D µCT

View Article Online
DOI: 10.1039/D5TA07792C

volume proportionally to the normalized intensity, resulting in a spatial zinc volume map. Porosity was calculated voxel-wise according to the equation below:

$$\theta = 1 - \frac{(1 - \theta_{GF}) \cdot dV + V_{3D\_zinc}}{dV} \quad (6)$$

where θ_{GF} is the initial porosity of the felt, V_{3D_zinc} is the zinc volume in the voxel, and dV is the voxel volume. Although the original voxel resolution was 22.19 micrometers, for statistical evaluation the data was aggregated into blocks of 100 × 100 × 4 voxels, resulting in an effective voxel size of approximately 2.2 mm × 2.2 mm × 0.1 mm.

Finally, porosity values were averaged across XY slices spanning the electrode thickness, from the membrane to the current collector, to observe spatial trends and correlate them with the state of charge and structural changes in the electrode.

2.4 Pressure half-cell tightness test

To assess the tightness of the battery half-cell, a pressure decay test was carried out in a specialized set-up (see **Figure S4**). One of the half-cells was pressurized by nitrogen applying a selected overpressure (in the range of 100-600 mbar), then the hydraulic circuit was closed, and a decay of the internal pressure was monitored by the pressure sensor. The internal tightness of the battery was assessed from the slope of pressure decrease in time evaluated from the 5-minute interval measurement.

View Article Online
DOI: 10.1039/D5TA07792C

3. Results

The primary aim of this study was to obtain a better understanding of the phenomena which are taking place during the operation of ZIHFB, particularly during its charging at increased Q_{areal}, leading to irreversible degradation of the battery performance. The result section is divided into three parts: i) identification of the individual degradation phenomena, ii) testing methods for battery performance recovery and the mitigation of the degradation process, and iii) identification of safe operating conditions providing stable and efficient battery performance at the mid-term time scale.

3.1 Voltaic bulge

3.1.1 Existence of voltaic bulge in ZIHFB

In this section we present the experiments in which the ZIHFB single-cell was cycled with a stepwise increasing SoC charging limit (to 20, 40, 60, and 80% of the theoretical capacity of the negolyte, volume of 0.07 mol dm^{-3}) in order to assess the maximum Q_{areal} still providing efficient and stable operation. Subsequently, several dozen charge-discharge cycles were performed with 80% SoC charging limit.

First, at low SoC charging limits, (20 and 40% SoC) the battery achieved high efficiencies (see **Table 1**), *CE* above 98% and *EE* above 85%. *EE* started to decrease during cycling with 60% SoC charging limit, but the *CE* still remained above 98%. The decrease of the *EE* was primarily caused by increasing charging voltage around 100 mAh cm^{-2} (corresponding to approx. 50% SoC of negolyte). When increasing charging limit to 80% SoC (~150 mAh cm^{-2}) a sharp increase of the cell voltage appeared followed by its sudden drop, demonstrating as a voltaic bulge around 125 mAh cm^{-2} (see **Figure 1a**). After the bulge, the charging voltage remained relatively high, around 1.5 V until the end of the charging half-cycle. Interestingly, the initial discharge voltage was about 100 mV lower than for 60% SoC charging limit, suggesting increased internal resistance of the discharging cell. Resulting *CE* of the cycle was significantly lower (by 9%) when compared to lower charging SoC limits. As visible from **Figure 1a** an available discharge capacity was only slightly higher than the value corresponding to the position at the end of the bulge on the x-axis, despite the fact that the cell discharging included a potentiostatic step at low cell voltage of 0.1 V. This indicates that some irreversible processes happened during the previous charging. During the subsequent battery cycling within the same SoC range, the voltaic bulge on the charging voltage profile gradually disappeared (see **Figure 1b, c**). Nonetheless, *CE* continuously decreased from 85% to 70% (see **Figure 1d**). Additionally, we observed a frayed charging voltage profile appearing at the bulge position, indicating an internal short circuit of the battery (see green curve in **Figure 1c**). The observed *CE* decay can be, to some extent, caused by a change of electrolyte composition and volume due to the observed net-flow through the CEM by osmosis and electro-osmosis (detailed description of expected ion fluxes in our system is further in this chapter). However, the main cause of performance deterioration seems to be most likely linked to the failure of inner cell components.

View Article Online
DOI: 10.1039/D5TA07792C

Table 1: Mean efficiencies and capacity utilization values. **Experimental conditions:** Std. electrolyte composition; Electrolyte volume: 0.07 dm^3 negolyte, 0.08 dm^3 posolyte; Current density of 100 mA cm^{-2}. Operating temperature: 40 °C; Electrolyte flow rate: 0.08 dm^3 min^{-1}.

SoC charging limit	Number of cycles	*CE*	*VE*	*EE*	*CU*
	-	%	%	%	%
20% SoC	5	99.1	84.5	83.7	20
40% SoC	5	98.8	85.4	84.4	40
60% SoC	5	98.7	78.4	77.4	59
80% SoC	5	89.4	76.4	68.2	72
80% SoC	49	77.0	78.0	60.0	67

a)

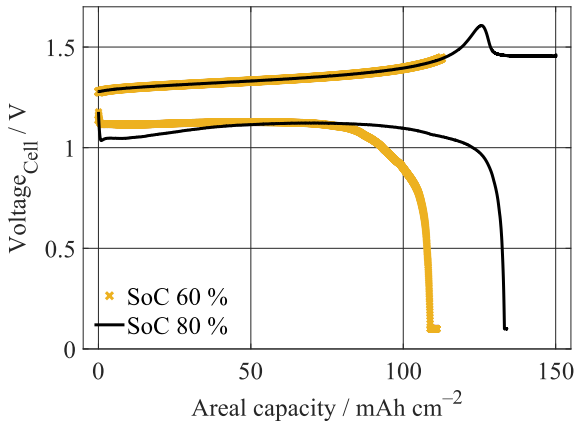

b)

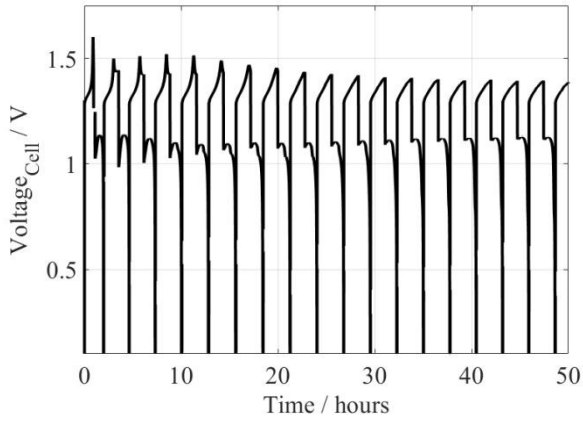

c)

d)

View Article Online
DOI: 10.1039/D5TA07792C

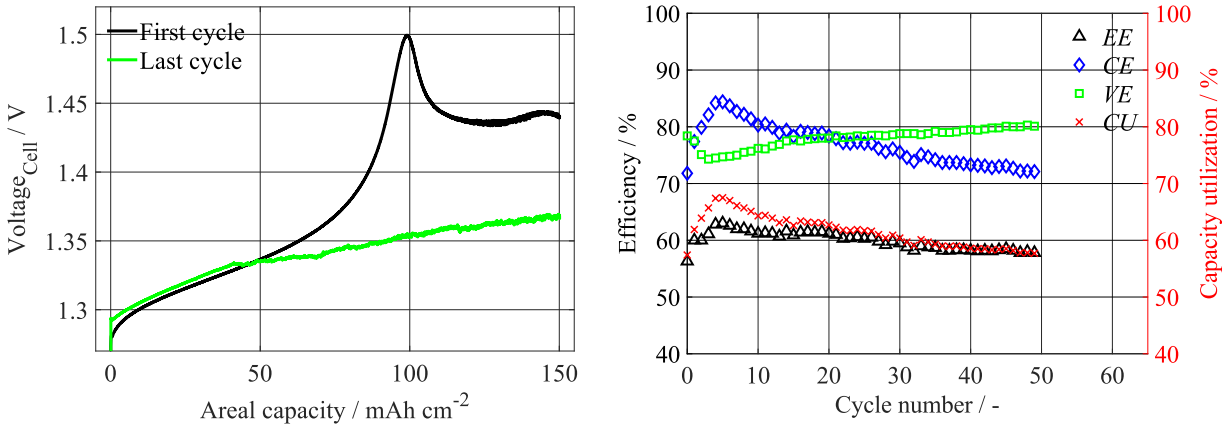

Figure 1: a) U-Q_{areal} dependence for 60% and 80% SoC charging limit. Subsequent battery cycling (49 cycles) with 80% SoC charging limit: **b)** Cell voltage development during initial 20 cycles; **c)** U-Q_{areal} dependence comparing charging for 1st and last cycle. **d)** Evolution of efficiencies and *CU*. **Experimental conditions:** Std. electrolyte composition; Electrolyte volume: 0.07 dm^3 negolyte, 0.08 dm^3 posolyte; Current density: 100 mA cm^{-2}: Operating temperature: 40 °C; Electrolyte flow rate: 0.08 dm^3 min^{-1}.

3.1.2 Expected ion fluxes in our ZIHFB

For the sake of better understanding of the voltaic bulge in the battery, we provide a detailed discussion of the expected fluxes of the individual electrolyte constituents (ions and water) which play significant role in the observed degradation mechanism and, thus, it is important to describe them specifically for our electrolyte composition (i.e., beyond the discussion in **Introduction**).

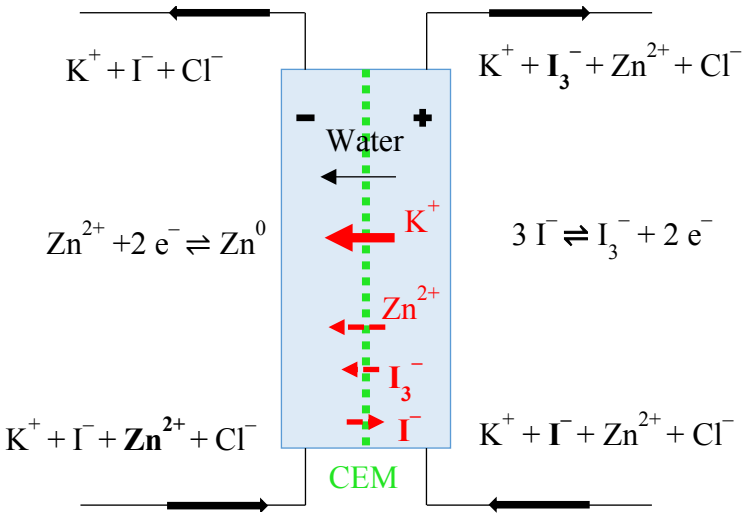

Figure 2: Expected cross flow of ions during ZIHFB charging for initial equal electrolyte composition.

In a ZIHFB cell employing a CEM, potassium ions serve as the primary charge carriers. During battery charging, they migrate, accompanied by water molecules in their hydration shells, from the posolyte to the negolyte under the influence of the electric field [34] to maintain electroneutrality in the electrolytes. A minor flux of Zn^{2+} ions to the negolyte may also occur, however, this contribution is significantly smaller due to their larger size [34]. In the positive half-cell, iodides are oxidized to tri-iodides. The reduced concentration of iodides in posolyte promotes their diffusion from the negolyte, whereas tri-iodide ions can diffuse in the opposite direction. Nevertheless, the transport of both anions is strongly suppressed by the CEM due to its high

View Article Online
DOI: 10.1039/D5TA07792C

selectivity and Donnan exclusion. During the charging, water is transported predominantly to the negolyte, driven by both electro-osmotic drags associated with K^+ migration and osmotic pressure differences arising from compositional changes during charging (schematics of all fluxes are captured on **Figure 2**). Although all fluxes theoretically reverse during discharge, complete compensation of species transport is rarely achieved in practice and the extent of reversal strongly depends on operating conditions, incl. the ratio of charging to discharging current densities (which governs migration), the duration of idle periods, and SoC range used for the battery cycling. Consequently, the volumes of the negolyte and posolyte change dynamically during battery operation. Importantly, because the charging processes are not fully efficient (due to self-discharge, parasitic hydrogen evolution reaction, passivation etc.), the net ionic and water flux through the CEM is biased towards the charging direction. Thus, over extended cycling, this imbalance leads to progressive electrolyte overflow towards the negolyte.

3.1.3 Structural analysis of negative 3D electrode

When analysing the negative felt electrode after the std. deposition to 80% SoC (negolyte volume of 0.06 dm^3, Q_{areal} of 129 mAh cm^{-2}), the zinc was visibly deposited on both sides of the GF, i.e., on the side facing the current collector (see **Figure S5b**) as well as on the side facing the membrane (see **Figure 3a**). The zinc distribution within the GF obtained via detailed µCT characterization (see **Figure 3b**, **c**) confirmed its dominant deposition within a relatively thin region neighbouring the membrane. The compactness of the layer on the current collector side is clearly visible from confocal laser optical microscopy images (**Figure 3c**). Some holes are also present within the layer (see red arrow), showing that the fibres of GF are compactly covered by Zn layer.

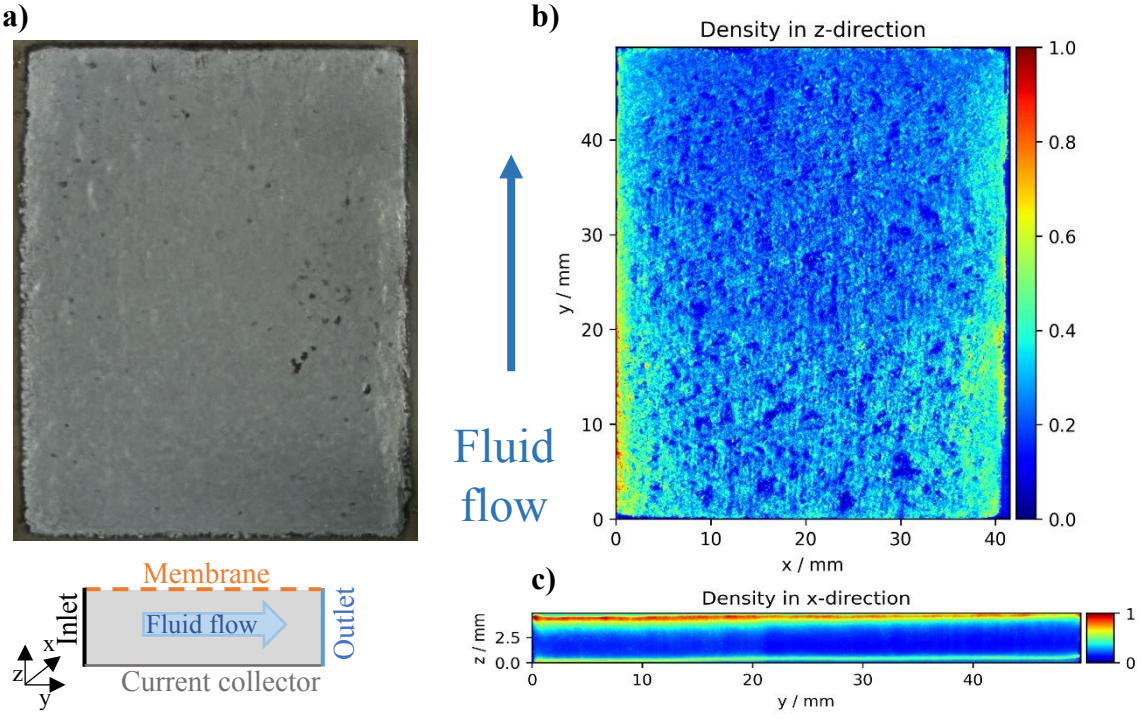

View Article Online
DOI: 10.1039/D5TA07792C

d)

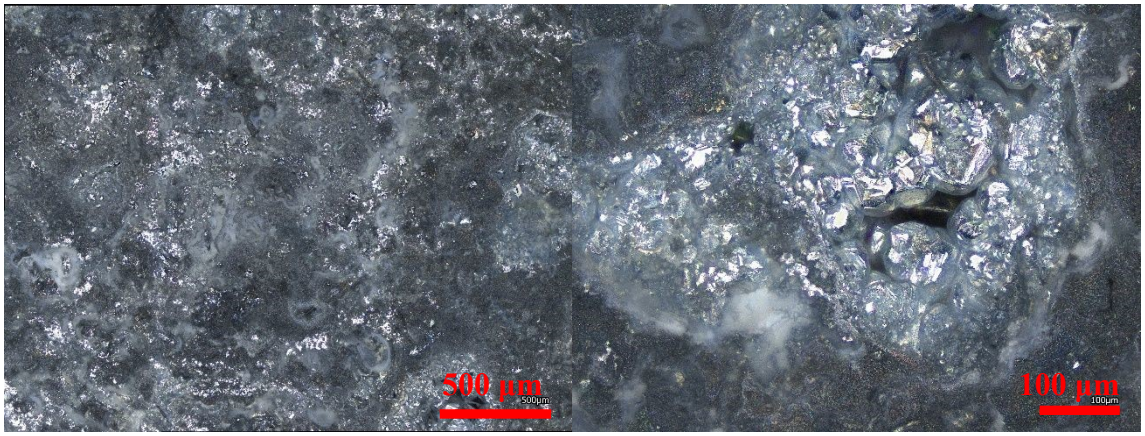

Figure 3: a) Photography of GF covered with zinc on the membrane side; µCT reconstruction in **b)** z- and **c)** x-direction showing the Zn distribution within GF electrode. **d)** A detail of a confocal laser microscopy image showing the compact zinc layer deposited at the electrode-membrane interface.

The preferential distribution of Zn close to the membrane is due to the fact that the electronic path within the GF is by order of magnitude more conductive (1100 mS cm^{-1} [35], depending on the relative compression) when compared to the ionic conductivity of the electrolyte (300 mS cm^{-1}). Thus, electric charge is preferentially transported in the form of electrons to the membrane proximity, where it is transferred from carbon fibres to an electrolyte via electrochemical reaction of Zn deposition. As expected, more zinc is deposited at the inlet of the GF due to the higher local concentration of Zn^{2+} reactants in the inlet region, which are being gradually consumed by the charging reaction. More importantly, excessive Zn deposition close to the membrane gradually decreases the effective area available for ionic transport through the membrane required for maintaining the electrolytes electroneutrality, as it was discussed in the previous chapter. µCT analysis revealed that the negative electrode porosity in the region near the membrane (0–0.09 mm) decreased from 0.935 (initial porosity of the GF according to [36]) to ~0.30 (under the conditions without observable voltaic bulge) and further to 0.15 under bulge conditions. This is consistent with the observed increase in ASR_{CT} due to reduced ionic transport through this progressively thicker and more compact layer adjacent to the membrane. The more detailed discussion is presented in **section S1** (and **Figure S6**) in the SI.

At a certain Q_{areal} the transport of the ions becomes limited by the created compact zinc layer on the GF-membrane interface and thus the overpotential of the cell steeply increases. Once the peak overvoltage is achieved it starts to decline, most probably due to gradual piercing of the CEM by Zn dendrites which are growing from the compact Zn layer towards the positive electrode. Interestingly, the cell voltage does not drop to zero (nor close to this value), which would be expected for a short-circuited cell, but it only decreases to a value slightly below 1.5 V. This can be explained by immediate exposure of zinc dendrites to tri-iodide ions contained in the charged posolyte), which effectively dissolves these temporary shorts. This so-called self-healing effect in ZIHFB has been described by Xie et al. [29] for the cell configuration using a porous separator, where it was effectively preventing a short-circuit of the cell. In contrast, for a cell using homogeneous CEM, the growing Zn dendrites can pierce the membrane (much thinner and more compact compared to the separator) resulting in the membrane perforation and battery

View Article Online
DOI: 10.1039/D5TA07792C

performance deterioration. The presence of tri-iodides in posolyte thus has no longer self-healing effect as it was reported for cells using a porous separator.

Overall, the gradual accumulation of Zn within the thin compact layer near the membrane, associated with decrease in negative electrode porosity, and resulting ionic transport limitation leads to a sharp increase in ASR_{CT}, membrane perforation by growing dendrites, and eventual irreversible performance deterioration.

3.2 Detailed study of the voltaic bulge

To further investigate the origins of the voltaic bulge, the reference electrodes were positioned on the outlet of both half-cells, allowing on-line monitoring of both electrodes' potentials during the battery testing. The potentials were recalculated to the normal hydrogen electrode (NHE). In **Figure S7**, we can see that during the battery charging within the voltaic bulge capacity region , electrode potentials showed only a minor change in their trends, not proportional to the increase in observed cell voltage. This can be illustrated by a difference between measured cell voltage (yellow curve) and the calculated difference between both electrodes' potentials (purple curve). This suggests that the increased cell overvoltage is associated with some processes related to the CEM rather than electrodes.

At first, we wanted to confirm that the presence of a voltaic bulge is not a function of electrolyte SoC (i.e., composition). Thus, we have performed a single charge-discharge experiment with two different volumes of negolyte: i) std. negolyte volume of 0.07 dm^3 (Q_{areal} of 150 mAh cm^{-2}) and; ii) decreased volume of 0.05 dm^3 (Q_{areal} of 107 mAh cm^{-2}). As expected with the decreased negolyte volume, we did not observed signs of the voltaic bulge (see **Figure 4a**) when charging to the same SoC limit (80% of the negolyte´s theoretical capacity). We have compared ASR_{Ω} and ASR_{CT} evaluated from EIS measurements performed at various SoCs within these experiments. We can see that at the beginning of the charging, ASR_{Ω} slightly decreases for both negolyte volumes, but furthermore, a significant increase of ASR_{CT} occurs only for the standard (higher) negolyte volume (see **Figure 4b**). In contrast, with the lower negolyte volume, there is only a minor ASR_{CT} increase at the really end of the charging. For lower negolyte volume, both *ASRs* remain almost constant during the whole discharge period, and they increase only at the end of discharging (see **Figure 4c**). Based on these observations, we can clearly state that voltaic bulge is not function of electrolyte composition but is directly related to the amount of the deposited Zn. For the std. negolyte volume the development of *ASR*s is significantly different and will be further discussed within this chapter. Note: As described in previous paragraphs, the increased cell polarization is only partially related to electrode processes (shown in **Figure S7**). Thus, also observed changes in the ASR_{CT}, i.e., impedance at medium frequency range most likely originates from a complex interplay of several processes, as will be further discussed. Despite that, for the sake of simplicity, we will refer to them as ASR_{CT}.

View Article Online
DOI: 10.1039/D5TA07792C

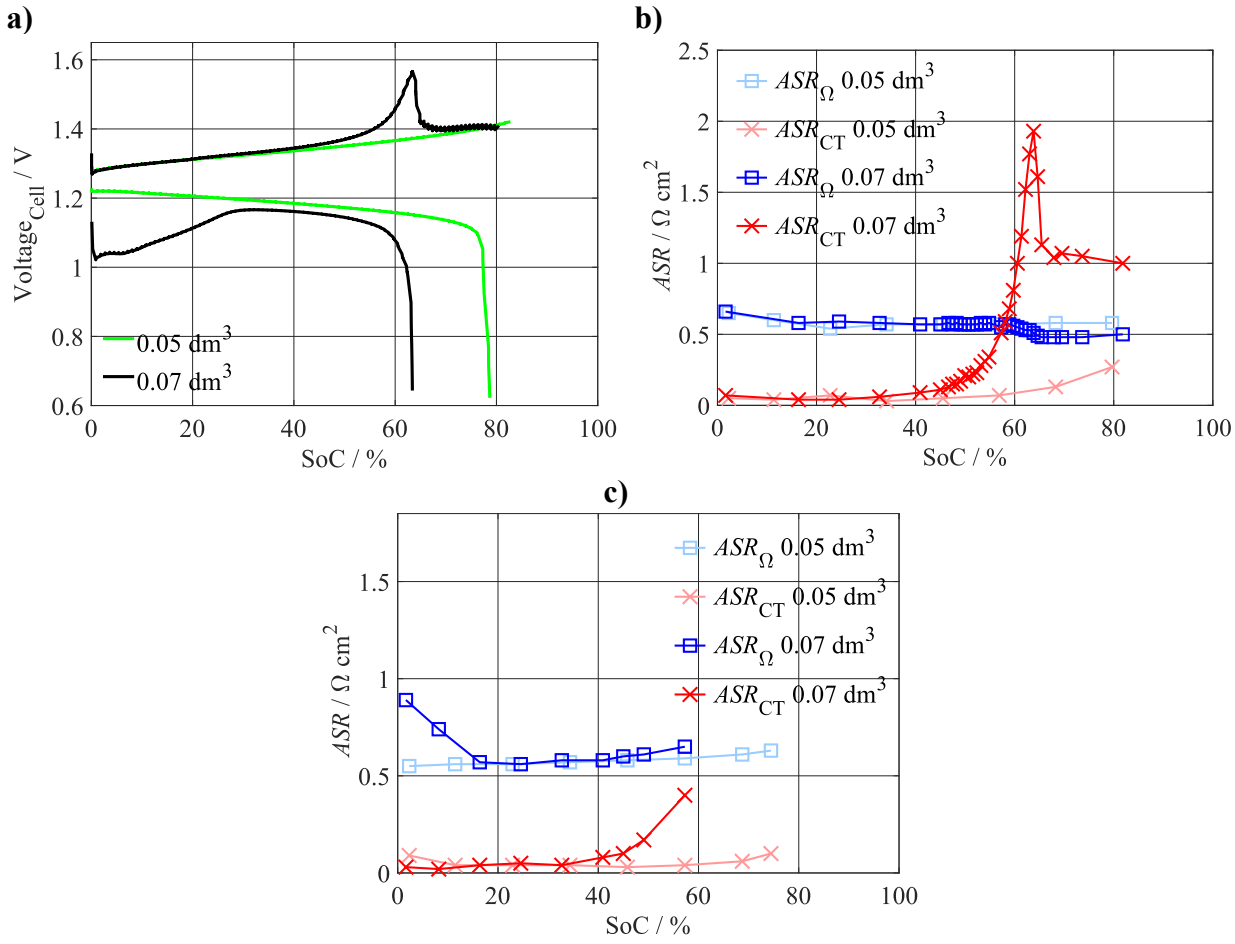

Figure 4: a) U-Q_{areal} dependence of a charge-discharge cycle for two different negolyte volumes with the same 80% SoC charging limit; ASR_{CT} and ASR_{Ω} evaluated from $GEIS_{LOAD}$ measured during the battery for **b)** charging and **c)** discharging phase of the initial cycle. **Experimental conditions:** Std. electrolyte composition, Current density: 100 mA cm^{-2}; Operating temperature: 40 °C; Electrolyte flow rate: 0.08 dm^3 min^{-1}.

Detailed characterization of the voltaic bulge for std. negolyte volume was carried out by a stepwise charging, where between each charging step (approx. 1.5 mAh cm^{-2} within the region of the voltaic bulge) the $PEIS_{OCV}$ was measured. In the **Figure 5a** we can see that the charging voltage in the region of the bulge is significantly higher when compared to the std. charging (i.e., CC charging without frequent EIS measurements), while the discharged capacity is even further decreased, resulting in a low *CE* of only 70%. This is probably due to a longer pause between charge and discharge part of the cycle and also pauses during which the $PEIS_{OCV}$ was measured (each $PEIS_{OCV}$ measurement required more than 10 minutes, i.e., whole charge-discharge cycle took more than 13 hours, while the std. cycle took only 3 hours). Interestingly, for a given Q_{areal} we observed significant variation of the EIS spectra in time (see **Figure S8**). This is most probably linked with the surface passivation of zinc deposited at the negative electrode; however, more detailed study is needed to confirm the hypothesis, which is beyond the scope of our study. Additionally, the quality of EIS spectra was significantly decreased at higher Q_{areal} (specifically at low frequencies region), due to insufficient stability of the system. Therefore, the $PEIS_{OCV}$ characterization was found unsuitable for our purposes. Interestingly, we observed a visible drop of OCV_{Cell} (see red curve in **Figure 5b**), although relatively small (approx. 14 mV), starting at the

View Article Online
DOI: 10.1039/D5TA07792C

Q_{areal} corresponding to the voltaic bulge peak, suggesting changes in the composition of the electrolyte and/or electrodes. The observed decrease in OCV_{Cell} can be attributed to the membrane damage, which allows direct exposure of the deposited zinc to the posolyte containing tri-iodides, leading to enhanced self-discharge. However, since the majority of zinc electrode remains intact and the bulk negolyte composition is largely preserved, the overall change in OCV_{Cell} remains rather small.

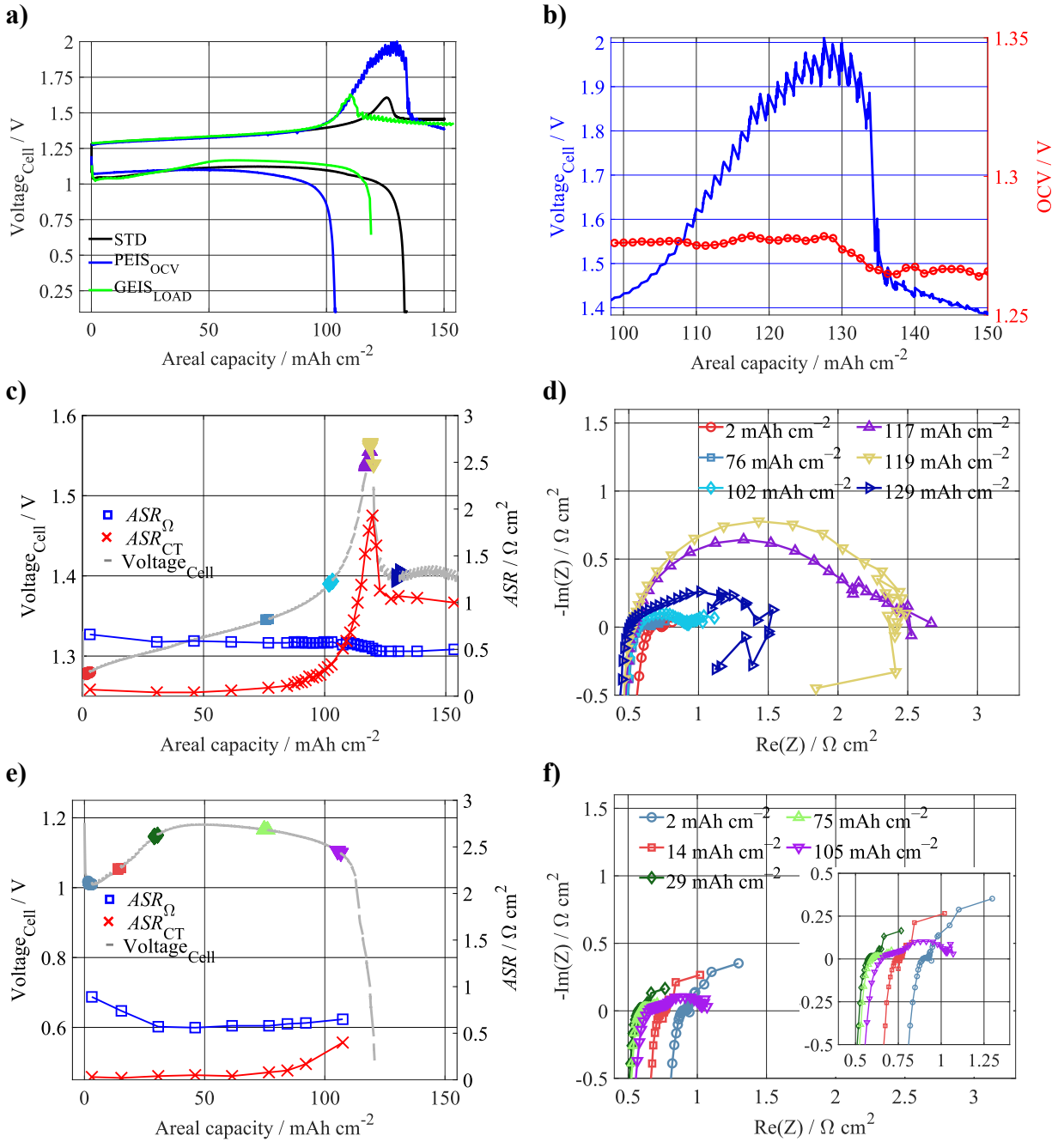

Figure 5: a) U-Q_{areal} dependence of a charge-discharge cycle for different characterization techniques: STD, $PEIS_{OCV}$, and $GEIS_{LOAD}$. **b)** OCV_{Cell}-Q_{areal} dependence during $PEIS_{OCV}$ characterization. **c)** U-Q_{areal} dependence during $GEIS_{LOAD}$ characterization with evaluated ASR_{CT} and ASR_{Ω}, colours used in the voltage cell evolution are linked to the

View Article Online
DOI: 10.1039/D5TA07792C

d) where EIS spectra are displayed with colour for corresponding Q_{areal}. Figures **e)** and **f)** represent the same as **c)** and **d)**, but for battery discharge. **Experimental conditions:** Std. electrolyte composition, Electrolyte volumes: 0.07 dm^3; Current density: 100 mA cm^{-2}; Operating temperature 40 °C; Electrolyte flow rate: 0.08 dm^3 min^{-1}.

To mitigate the influence of battery behaviour instability during $PEIS_{OCV}$ measurements, $GEIS_{LOAD}$ was performed under constant current density load. The $GEIS_{LOAD}$ technique allows to measure the EIS spectra at the same time as CC charging/discharging of the battery, i.e., suppressing the effect of zinc electrode changes during the periods without current loading. **Figure 5a** compares the cell voltage profiles for standard (STD) charging, $PEIS_{OCV}$, and $GEIS_{LOAD}$. The overvoltage development observed during $GEIS_{LOAD}$ closely resembles that of STD charging conditions. However, the voltaic bulge appeared even at lower Q_{areal}, which may be attributed to the alternating current applied during the $GEIS_{LOAD}$ measurement (i.e., current densities oscillated around 100 mA cm^{-2}). Nevertheless, the bulge´s position varied slightly across the measurements even under std. conditions, typically occurring between 115 and 130 mAh cm^{-2}, thus both STD and $GEIS_{LOAD}$ experiments can be considered comparable.

More importantly, a significant increase in the ASR_{CT} is observed for the $GEIS_{LOAD}$ experiment (see **Figure 5c**, **d**), starting around 130 mAh cm^{-2}. The ASR_{CT} peak position aligns with the overvoltage maximum, and it subsequently decreases, stabilizing at approximately 1 Ω cm^2. In contrast, ASR_{Ω} gradually decreases in the same capacity region, with the most pronounced drop occurring near the voltage peak, after which it remains relatively constant. The decreased ASR_{Ω} aligns well with the hypothesis that the membrane is pierced by Zn dendrites.

Interestingly, the presence of voltaic bulge also affects the battery overvoltage at the beginning of subsequent discharging. **Figure 5e** shows a significant drop of battery voltage during initial discharging phase, caused by ASR_{Ω} increase (blue curve, compared to the ASR_{Ω} at the end of charging), probably due to zinc electrode passivation (most probably related to the presence of tri-iodide ions). During the subsequent battery discharge, ASR_{Ω} decreases back to 0.6 Ω cm^2 after approx. 25 mAh cm^{-2} and, further on, the discharge voltage is similar to the experiment with the lower volume of negolyte (see **Figure 4a**). ASR_{CT} increases when the battery is almost fully discharged, i.e., zinc is almost fully dissolved.

To test the integrity of the membrane after the cycling a tightness test was applied (after ZIHFB single-cell was emptied). One of the half-cells of the ZIHFB was pressurized by nitrogen, then hydraulically closed and the rate of its pressure decay was monitored. In an initial cell with a fresh membrane, the pressure decayed at a slow rate of approx. 0.01 mbar s^{-1} even under an overpressure of 600 mbar. In contrast, for the cell after the experiments we observed significantly faster pressure drops of 0.32 mbar s^{-1}, indicating a decreased membrane tightness, most probably due to its perforation by Zn dendrites.

3.2.1 Influence of electrolyte composition: ZnI_2 omission in posolyte

The composition of flow battery electrolytes plays a significant role in energy density, efficiency, and stability of storage. In ZIHFB, Zn^{2+} ions are, in theory, only needed in the negolyte while iodides in the posolyte. However, in practice, the mixed electrolyte concept is typically used, containing both discharged active species in both electrolytes, which provides the battery with a favourable option of electrolyte remixing to restore their initial composition.

View Article Online
DOI: 10.1039/D5TA07792C

To further deepen our insight into the phenomena related to voltaic bulge, we performed a similar set of experiments, but with ZnI_2 omitted from the posolyte. In the $PEIS_{OCV}$ experiment, we observed that the battery voltage during the charging increased earlier approx. at 100 mAh cm^{-2} and a sudden voltage drop occurred later (purple curve in **Figure 6a**) compared to the standard operation with Zn^{2+} in both electrolytes (black curve). Moreover, the behaviour of the OCV_{Cell} also differed: instead of stabilizing, the OCV_{Cell} continued to rise and only dropped when the overvoltage decreased (see **Figure 6b**). Since Zn^{2+} ions were absent in the posolyte for this experiment, they could not be supplied to the negative half-cell during the charging, unlike in the standard electrolyte set-up. At higher Q_{areal}, when the GF is plated with a compact zinc layer preventing the ions transport to the significant part of the electrode, the additional supply of Zn^{2+} from the posolyte is missing, which, in turn, results in a premature voltage increase in case of the $PEIS_{OCV}$ experiment.

However, in the case of $GEIS_{LOAD}$ cycling, the absence of Zn^{2+} in the posolyte appears to delay the voltaic bulge, shifting it to higher Q_{areal} values (~150 mAh cm^{-2}), see **Figure 6a**, when compared to both standard operation (black curve, with Zn^{2+} in posolyte and without frequent EIS measurement) and $PEIS_{OCV}$. Although ASR_{Ω} remains approximately constant at the onset of the bulge, ASR_{CT} sharply grows in this region (see **Figure 6c**). However, ASR_{CT} does not decrease significantly with the voltage drop – only its slight reduction is observed. This behaviour can be explained by partial membrane penetration by Zn dendrites (reflected in the decreased ASR_{Ω}) and partial zinc dissolution by tri-iodide ions. However, since Zn^{2+} are absent in the posolyte, the Zn deposition cannot proceed in the positive half-cell, as it was possible for the standard electrolyte configuration, and thus ASR_{CT} stays constant.

In general, the absence of Zn^{2+} in the posolyte allows pushing the voltaic bulge to higher Q_{areal} and also to reducing discharge overvoltage (see **Figure 6a**). However, at the same time, different initial composition of the posolyte and negolyte would inevitably lead to the earlier battery failure, primarily due to a significant cross-over of water, active species, and other ions through the membrane, which gradually changes the electrolytes composition (electrolyte volume disbalance is demonstrated in **Figure S9**). The fluxes for symmetrical electrolyte composition are discussed in **section 3.1.2.** In principle, the behaviour in this modified configuration will remain similar; however, as mentioned in the beginning of this section, with the initially equal electrolyte composition the capacity fade due to membrane cross-over can be easily recovered by simple remixing of the electrolytes. For the posolyte without ZnI_2, this measure is no longer possible.

View Article Online
DOI: 10.1039/D5TA07792C

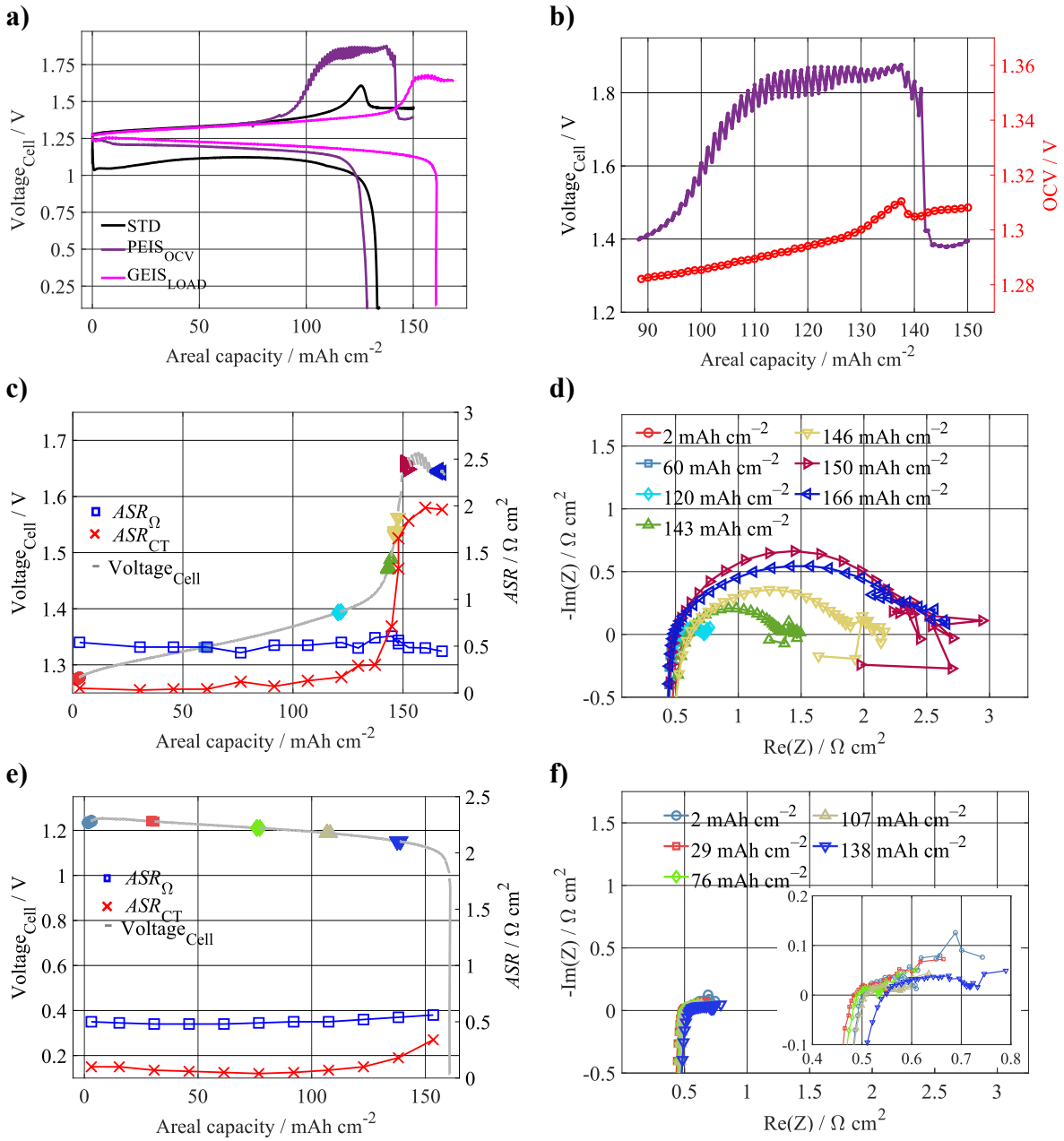

Figure 6: a) U-Q_{areal} dependence of a charge-discharge cycle for different characterization techniques STD, $PEIS_{OCV}$ and $GEIS_{LOAD}$ for ZIHFB with omitted zinc ions in posolyte (besides STD). **b)** OCV_{Cell} dependence on Q_{areal} during $PEIS_{OCV}$ characterization. **c)** U-Q_{areal} dependence during $GEIS_{LOAD}$ characterization with evaluated ASR_{CT} and ASR_{Ω}, colours used in the voltage cell evolution are linked to **d)** where EIS spectra are displayed with colour for corresponding Q_{areal}. Figures **e)** and **f)** represents the same as **c)** and **d)**, but for battery discharge. **Experimental conditions:** Std. negolyte composition, ZnI_2 omitted from posolyte (besides STD); Both electrolytes' volumes 0.07 dm^3.

3.3 Strategies for capacity regeneration

Subsequently, with the degraded battery we tested several strategies that are typically used for a RFB to restore its initial capacity, namely: i) electrolyte remix, ii) exchange of both electrolytes for the fresh ones and iii) exchange of the CEM (while keeping same electrolytes). In this series of experiments, the volume of electrolytes was decreased to 0.06 dm^3.

View Article Online
DOI: 10.1039/D5TA07792C

Electrolyte remixing and exchange

The first strategy tested for regenerating the battery performance was mixing the posolyte and negolyte and redistributing them. This procedure for regenerating the initial composition of the electrolytes is possible thanks to their initial equal composition. Electrolyte remix was done after complete ZIHFB discharge and whole procedure is described in detail in the **subchapter** in **section 2.2.3**.

During the subsequent battery cycling, *CE* remained low, even for lower SoC charging limits (started from 40% SoC, see **Figure 7a**). Interestingly, in the first cycle after the electrolyte remix, a low charging voltage was observed i.e., short plateau at 0.1 V at the beginning of charging, (0 - 5 mAh cm^{-2}, see **Figure S10**), which was caused by the reduction of tri-iodide ions at the negative half-cell. The tri-iodide presence in the remixed negolyte was a consequence of faradaic imbalance between both electrolytes before the remix due to the coulombic inefficiency of the negative half-cell reaction (HER side reaction, self-discharge due to Zn corrosion) and accumulation of tri-iodide ions in the discharged posolyte. Even after a complete electrolyte exchange for the fresh electrolytes, the original *CE* was not restored (depicted on right side of **Figure 7a**), which indicate a CEM damage to be responsible for irreversible performance fade.

Membrane exchange

To confirm the CEM damage, we repeated the experiment described above with a fresh electrolytes and new cell. The procedure involved initially increasing the SoC until the characteristic voltaic bulge appeared. Following this, the battery was fully discharged, and the electrolyte was remixed, as previously outlined. Then, the used CEM was replaced with a fresh one, while leaving the rest of the battery components unchanged (incl. GFs and both electrolytes). In **Figure 7b** we can see that the CEM replacement led to a substantial recovery of the *CE* to 90%, clearly proving that the membrane degradation is mostly responsible for cell performance degradation related to the voltaic bulge. However, during subsequent cycling the *CE* dropped again, as already in the second cycle the voltaic bulge was observed (despite the charging voltage cut-off limit was set to 1.55 V), resulting again in the CEM damage and gradual discharge capacity decrease. Lower *CU* after electrolyte exchange was caused by presence of tri-iodide ions in the remixed negolyte, as discussed in the previous section.

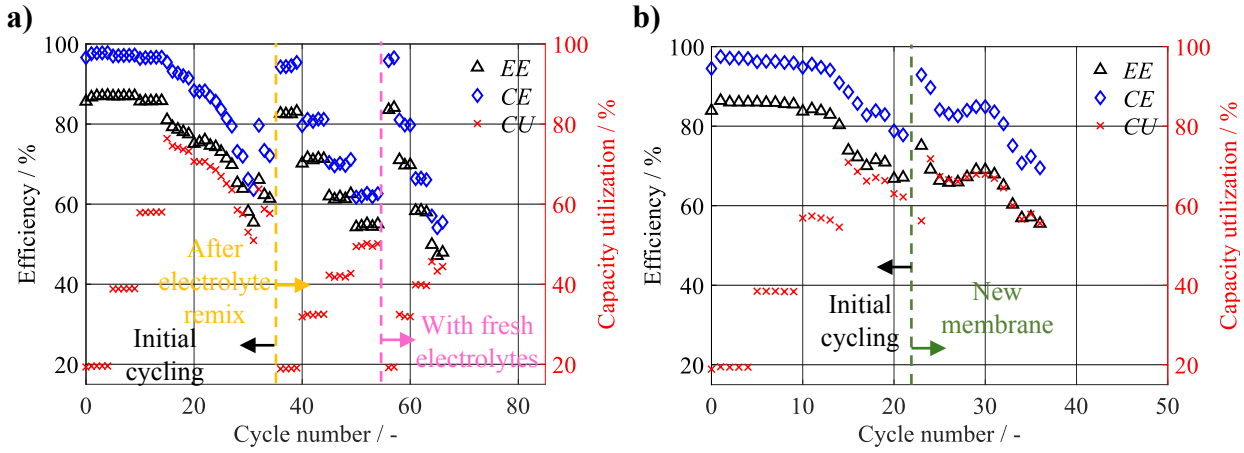

View Article Online
DOI: 10.1039/D5TA07792C

Figure 7: Efficiencies and *CU* development **a)** for the experiment in with remix of the electrolyte and exchange of the electrolytes and **b)** for the experiment in with CEM exchange. **Experimental conditions:** Std. electrolyte composition; Electrolytes volumes: 0.06 dm^3; Current density: 100 mA cm^{-2}; Operating temperature 40 °C; Electrolyte flow rate: 0.08 dm^3 min^{-1}.

3.4 Construction modifications

Based on our findings that the voltaic bulge is caused by deposition of a compact zinc layer close to the electrode-membrane interface and the consequent perforation of CEM by Zn dendrites, we have tested several protection construction modifications of battery cell and experimental set-up aiming to mitigate the unwanted degradation mechanism and to increase Q_{areal} securing stable and efficient battery operation.

3.4.1 Non-conductive felt

Kellamis et al. [21] used NCF to increase the Q_{areal} of the ZIHFB operation and prevent short-circuits. We focused on a similar approach by combination of electronically conductive GF and NCF (polymeric non-conductive felt, FINET PES 1 mm, MITOP) in each half-cell, separately, in order to see the effect of this construction modification on the cell behaviour at increased Q_{areal} aiming to at least partially suppress this phenomenon or to postpone it to higher Q_{areal}. The NCF was always located in a direct contact with the CEM, which was supposed to provide better protection of the membrane against Zn dendrites (for detailed schematics see **Figure S2**).

NCF in negative half-cell

Initially, the combination of GF and NCF (close to membrane) was used in the negative half-cell (for short NCF_{NEG}), so the initial deposition zone is more distant from the membrane (aiming to protect membrane). Surprisingly, the use of NCF_{NEG} reduced *CE* by 3-4 % for all the tested charging SoC limits (see **Figure 8a**,) when compared to std. battery construction (i.e., both half-cells using only conductive GF). This is probably a consequence of a nonhomogeneous growth of Zn in the NCF_{NEG} structure at relatively high applied current density (100 mA cm^{-2}), leading to its uneven distribution (photo of NCF_{NEG} after the cycling is shown in **Figure S11**) forming undesirable dendritic structures that are more susceptible to parasitic processes such as hydrogen evolution, Zn passivation and physical disintegration from electrode bulk. Thus, contrary to our expectations, the application of NCF_{NEG} did not suppress the voltaic bulge, nor it did not shift it to higher Q_{areal} (see blue curve in **Figure 8b**).

View Article Online
DOI: 10.1039/D5TA07792C

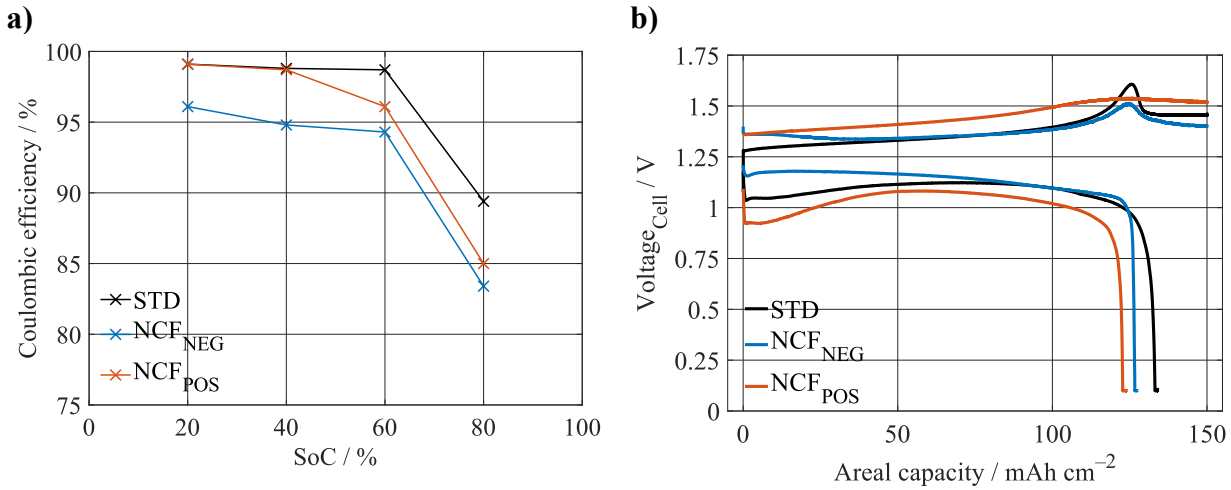

Figure 8: a) *CE* evolution for the std. construction and the experiment with the NCF_{NEG} and NCF_{POS} half-cell in the ZIHFB. **b)** ZIHFB voltage dependence on Q_{areal} for different construction modification (construction modification is captioned in **Figure S2**). **Experimental conditions:** Std. electrolyte composition: 0.07 dm^3 negolyte, 0.08 dm^3 posolyte; Current density: 100 mA cm^{-2}; Operating temperature 40 °C; Electrolyte flow rate: 0.08 dm^3 min^{-1}.

A possible explanation for the presence of voltaic bulge in the case of NCF_{NEG} is that a compact layer of zinc grows near the GF/NCF interface, which may have a similar insulating effect for ions transport between both half-cells of battery, increasing local current densities and, in turn, resulting in more pronounced zinc dendrites formation and CEM perforation. In contrast to std. cell construction, interestingly, there is no increase of overvoltage at the beginning of the discharging, which can be attributed to the fact that the compact zinc layer is located at the GF/NCF interface (i.e., not in a direct contact with CEM) and thus smaller portion of CEM cross-sectional area is blocked. Higher discharge voltage is demonstrated on increased *VE* by 5% (see **Table 2**). The voltaic bulge position occurs at approx. same Q_{areal} (i.e., 125 mAh cm^{-2}) as for std. electrode configuration suggesting that maximal capacity is limited by inner geometry of the cell rather than distribution of conductive and non-conductive phases in the negative half-cell.

NCF in positive half-cell

In the next experiment, a NCF was used in a positive half-cell (again facing the membrane, for short NCF_{POS}). According to Kellamis et. al. [21], this approach should mitigate electric short circuits and thus leads to increased Q_{areal}. In our experiment, the voltaic bulge was present (see **Figure 8b**) even though it was not that significant, its position was similar to the STD and NCF_{NEG} and irreversible reduction of the battery *CE* also occurred. The initial drop in discharge voltage was similar to a standard cell construction experiment, indicating that this effect is associated with the negative half-cell, since this voltage drop was absent in the NCF_{NEG} configuration. Due to the presence of a NCF_{POS} next to CEM, providing few mm thick electronically insulating zone, we can argue that the irreversibly reduced *CE* is not caused by std. internal battery short circuit, i.e., the electron-conductive connection of the two electrodes. More probably, the zinc growing through the membrane is being continuously dissolved by the I_3^- present in the posolyte. And this self-discharging process leads to a decreased *CE*, and its further gradual decrease due to the membrane perforation by Zn dendrites (after whose dissolution holes remain in the membrane). Alternatively,

View Article Online
DOI: 10.1039/D5TA07792C

some of the I_3^- may penetrate through these pores and dissolve also the zinc deposited in the negative half-cell.

Table 2 shows a generally lower *VE* of the NCF_{POS} cell due to the significant increase in ASR_Ω (EIS measured at 50% SoC) caused by the presence of the electronically insulating NCF. Interestingly, for the NCF_{NEG} experiment, such significant increase in ASR_Ω was not observed as, upon the charging, zinc is present within the negative electrodes structure (both in GF and NCF), which increases the initially low conductivity of the NCF layer. Initial charging overvoltage for both NCF experiments is similar, and it decreases with increasing Q_{areal} for the arrangement with NCF_{NEG} (see blue and orange curve in **Figure 8b**), which confirms that the deposited zinc compensates increased ASR_Ω.

Table 2: ASR_Ω evaluated from EIS measured in 50% SoC and average *CE*, *VE* evaluated from the cycling with different SoC charging limit. The experimental conditions are the same as those given for **Figure 8**.

	ASR_Ω	***CE*** **SoC 60 %**	***VE*** **SoC 60 %**	***CE*** **SoC 80 %**	***VE*** **SoC 80 %**
	Ω cm²	%	%	%	%
Standard	0.68	98.7	78.4	89.4	76.4
NCF_{NEG}	0.60	94.3	83.4	83.4	81.1
NCF_{POS}	1.54	96.1	70.9	85.0	69.6

Despite similar construction modifications used (NCF_{POS}) as in case of Kellamis et al. [21], we did not reproduce their increase of Q_{areal}, potentially because we used conductive GF in the negative half-cell instead of NCF_{NEG} as in the mentioned study. Other factors such as use of different electrolyte composition (they used $ZnCl_2$ and NH_4Br) may cause the difference. Additionally, if we look at their results, we can see that during the initial 10 cycles the available Q_{areal} decreased by more than 35% from the original 490 mAh cm^{-2}, due to the significant increase of charging voltage and presence of zinc oxide in the negative half-cell. Thus, a similar trend was observed as in our system: a significant increase in charging voltage consequently affecting the discharge voltage. Nevertheless, the battery was not permanently damaged, likely due to the implementation of a safety charging voltage limit.

3.4.2 Hydraulic connection of electrolyte tanks

Finally, we have identified stable operating conditions for the ZIHFB single-cell by combining a safety charging cut-off voltage and a reduced charging Q_{areal} limit (for detailed conditions see **subchapter** in **section 2.2.3**) with a hydraulic connection between the electrolyte tanks. HS was used to maintain equal electrolytes volumes and to at least partially equalize their composition via a thin capillary at the bottom of the tanks. This strategy is typically used in VRFB to keep constant electrolyte volumes, mitigating the capacity fade due to active species cross-over. [37]

View Article Online
DOI: 10.1039/D5TA07792C

In a ZIHFB with a CEM, the net ion and water flux during charging is directed from the posolyte to the negolyte, reversing during discharge, as discussed in **Section 3.1.2**. When a HS is present, the reverse flow through the HS partially compensates for these volume changes and, to some extent, mitigates composition imbalances during battery operation. However, this benefit comes at the expense of reduced *CE* due to increased self-discharge (zinc dissolution by tri-iodide ions transferred via HS from posolyte), however, this can, on the other hand, prevent excessive zinc accumulation and associated risks.

Firstly, the std. apparatus without HS of electrolyte tanks was used to study the effect of HS on operation of ZIHFB. Despite the safety limits applied, the operation of the battery without HS was unstable. As it is shown in **Figure 9a**, the battery exhibits a gradual decline in all efficiencies during CC cycling periods, which was probably attributed to the zinc accumulation (its incomplete dissolution during discharge periods), which caused the battery to operate at gradually increased SoC (of negolyte), leading to increased charging voltage. During the two formatting cycles (CC charge and combined CC-CV discharge), a steep recover in *CE* was observered, indicating that the accumulated zinc was effectively dissolved by potentiostatic discharge at 0.1 V. However, the improvement was only temporary as the voltaic bulge appeared after approx. 48 cycles (80 hours), and the battery was irreversibly degraded. Voltaic bulge appeared due to the changing electrolyte composition caused by noteworthy electrolyte cross-over (from posolyte to negolyte, shown in **Figure S12**).

Deployment of HS led to significant stabilization of the battery operation (see stable efficiency development in **Figure 9b**), due to continuous balancing of the electrolyte's volumes (and partially also of their composition). Most likely, part of the accumulated zinc was also being partially dissolved during discharge by the I_3^-, which were gradually transported to the negolyte via HS. In other words, continuous mitigation of zinc accumulation in the negative half-cell prevents overcharging of the battery (i.e., exceeding critical Q_{areal}) and protects against subsequent membrane damage. With these optimized conditions ZIHFB was operated at 100 mA cm^{-2}, achieving high performance demonstrated on *VE* and *EE* consistently above 80% while no significant performance deterioration was observed.

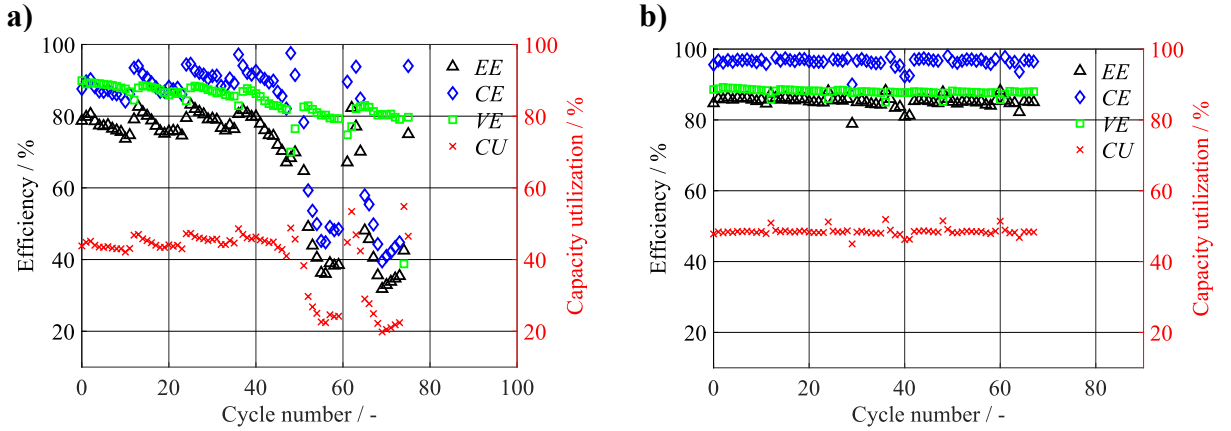

Figure 9: Comparison of efficiencies development in ZIHFB under optimized operation conditions **a)** without HS and **b)** with HS. **Experimental conditions:** Std. electrolytes composition; Electrolytes volumes: 0.06 dm^3; Charging

View Article Online
DOI: 10.1039/D5TA07792C

voltage limit 1.55 V; Q_{areal} capacity charge limit 80 mAh cm^{-2}; Current density: 100 mA cm^{-2}; Operating temperature 40 °C; Electrolyte flow rate: 0.08 dm^3 min^{-1}.

We found that from the mitigation strategies tested, a mid-term stable and efficient battery operation (at least in our configuration) can only be achieved by decreasing charging Q_{areal} limit (to 50% SoC, Q_{areal} 80 mAh cm^{-2}), applying a voltage charging limit (1.55 V) and, most importantly, by implementing HS construction modification for mutual connection of the electrolyte tanks. The achieved Q_{areal} of 80 mAh cm^{-2} at high current density of 100 mA cm^{-2} is higher when compared to most of the literature where the reported Q_{areal} values are between 40-60 mAh cm^{-2} [29, 34, 38, 39] for current densities no higher than 80 mA cm^{-2}. Only one study by Kellamis et al. [21], reported higher Q_{areal} (stable above 350 mAh cm^{-2}), thanks to use of NCF_{POS}, as was discussed in previous chapter. However, our configuration excels in high efficiencies (*EE* is higher by 24% in our configuration) and improved safety (bromine free) which can be used for power application with lower capacity.

Besides the promising performance parameters achieved, as mentioned above, the main contribution of our study is the proposed and experimentally validated mechanistic explanation of the voltaic bulge phenomenon and its consequences on the battery operation. These findings highlight the importance of further R&D of this system which should be aimed on the improved homogeneity of the Zn distribution within the 3D negative electrode, e.g., by variation of its surface chemistry, conductivity and texture in order to further increase Q_{areal} of the ZIHFB cell and to decrease the cost per capacity related to the battery stacks.

4. Conclusions

In this study, we investigated a degradation phenomenon in ZIHFBs, referred to as the voltaic bulge, which occurs when charging to high Q_{areal}. This effect manifests as a sharp voltage rise followed by a sudden drop, resulting in an irreversibly decreased *CE* of the charge-discharge cycle. Although the bulge gradually disappears upon further cycling, it is accompanied by irreversible damage to the ion-exchange membrane, requiring replacement to restore the initial battery performance. Our results suggest that, for the std. cell construction, the bulge originates from the formation of a compact zinc layer near the electrode-membrane interface, restricting ionic transport from positive to negative electrode and increasing local current densities at the negative half-cell, which promotes dendritic growth and membrane perforation. For our system, the phenomenon typically appears at a critical Q_{areal} of 115–130 mAh cm^{-2} and is promoted by presence of Zn^{2+} in the posolyte (i.e., for the equal initial composition of both electrolytes). Removing Zn^{2+} from the posolyte delays its onset to higher capacities, but it does not represent a viable long-term solution due to the mutual electrolytes cross-contamination and early battery failure. From the tested construction modifications, the application of non-conductive felt to individual half-cells did not increase the limiting Q_{areal}, while hydraulic connection of the electrolyte tanks significantly improved the performance stability within restricted SoC limits. Safe operating conditions were identified as a charging voltage limited to 1.55 V and maximum charging Q_{areal}, of 80 mAh cm^{-2}. The system with the optimized construction (HS) and operating conditions enabled stable cycling with $CE \geq 95\%$, $EE > 83\%$ at 100 mA cm^{-2} and a low-capacity

View Article Online
DOI: 10.1039/D5TA07792C

fade of 0.02% per cycle. Understanding this mechanism provides a basis for strategies to mitigate membrane degradation and improve the durability of ZIHFBs and related zinc-based chemistries.

Author contributions

Přemysl Richtr: writing – original draft, investigation, formal analysis, validation, methodology, conceptualization, data curation, writing – review & editing. **David Gráf**: investigation, visualization, writing – review & editing. **Martin Drnec**: investigation. **Jiří Charvát**: conceptualization, writing – review & editing. **Martin Bureš**: software, writing – review & editing, software. **Ondřej Navrátil**: conceptualization. **Jaromír Pocedič**: supervision, conceptualization. **Juraj Kosek**: project administration, funding acquisition. **Petr Mazúr**: project administration, supervision, funding acquisition, writing – review & editing, resources, conceptualization.

View Article Online
DOI: 10.1039/D5TA07792C

Acknowledgments

This work was supported by the project "The Energy Conversion and Storage", funded as project No. CZ.02.01.01/00/22_008/0004617 by Programme Johannes Amos Comenius, called Excellent Research.

This work was supported by TAČR, program TREND, project no. FW06010097.

This work was supported from the grant of Specific university research – grant A1_FCHI_2024_04 and A2_FCHI_2025_014.

View Article Online
DOI: 10.1039/D5TA07792C

1. Wang, L., et al., *Science mapping the knowledge domain of electrochemical energy storage technology: A bibliometric review.* Journal of Energy Storage, 2024. **77**: p. 109819.
2. Gür, T.M., *Review of electrical energy storage technologies, materials and systems: challenges and prospects for large-scale grid storage.* Energy & Environmental Science, 2018. **11**(10): p. 2696-2767.
3. Sánchez-Díez, E., et al., *Redox flow batteries: Status and perspective towards sustainable stationary energy storage.* Journal of Power Sources, 2021. **481**: p. 228804.
4. Arévalo-Cid, P., et al., *Redox flow batteries: a new frontier on energy storage.* Sustainable Energy & Fuels, 2021. **5**(21): p. 5366-5419.
5. Lourenssen, K., et al., *Vanadium redox flow batteries: A comprehensive review.* Journal of Energy Storage, 2019. **25**: p. 100844.
6. Mazur, P., et al., *Effect of graphite felt properties on the long-term durability of negative electrode in vanadium redox flow battery.* Journal of Power Sources, 2019. **414**: p. 354-365.
7. Skyllas-Kazacos, M. and J.F. McCann, *Chapter 10 - Vanadium redox flow batteries (VRBs) for medium- and large-scale energy storage*, in *Advances in Batteries for Medium and Large-Scale Energy Storage*, C. Menictas, M. Skyllas-Kazacos, and T.M. Lim, Editors. 2015, Woodhead Publishing. p. 329-386.
8. Cunha, Á., et al., *Vanadium redox flow batteries: a technology review.* International Journal of Energy Research, 2015. **39**(7): p. 889-918.
9. Leung, P., et al., *Progress in redox flow batteries, remaining challenges and their applications in energy storage.* RSC Advances, 2012. **2**(27): p. 10125-10156.
10. Noack, J., et al., *Techno-Economic Modeling and Analysis of Redox Flow Battery Systems.* Energies, 2016. **9**(8): p. 627.
11. Noack, J., et al., *Studies on Fe/Fe Redox Flow Batteries with Recombination Cell.* Journal of The Electrochemical Society, 2020. **167**(16): p. 160527.
12. Mahmood, A., Z. Zheng, and Y. Chen, *Zinc–Bromine Batteries: Challenges, Prospective Solutions, and Future.* Advanced Science, 2024. **11**(3): p. 2305561.
13. Fan, D., et al., *Progress and challenges of zinc-iodine flow batteries: From energy storage mechanism to key components.* Journal of Energy Storage, 2024. **92**: p. 112215.
14. Jang, W.J., et al., *Effect of an Iodine Film on Charge-Transfer Resistance during the Electro-Oxidation of Iodide in Redox Flow Batteries.* ACS Applied Materials & Interfaces, 2021. **13**(5): p. 6385-6393.
15. Dundálek, J., et al., *Zinc electrodeposition from flowing alkaline zincate solutions: Role of hydrogen evolution reaction.* Journal of Power Sources, 2017. **372**: p. 221-226.
16. Zhang, X.G., *SECONDARY BATTERIES – ZINC SYSTEMS | Zinc Electrodes: Overview*, in *Encyclopedia of Electrochemical Power Sources*, J. Garche, Editor. 2009, Elsevier: Amsterdam. p. 454-468.
17. Lu, W., et al., *Anode for Zinc-Based Batteries: Challenges, Strategies, and Prospects.* ACS Energy Letters, 2021. **6**(8): p. 2765-2785.
18. ShakeriHosseinabad, F., et al., *Influence of Flow Field Design on Zinc Deposition and Performance in a Zinc-Iodide Flow Battery.* ACS Applied Materials & Interfaces, 2021. **13**(35): p. 41563-41572.
19. Pichler, B., et al., *The impact of operating conditions on component and electrode development for zinc-air flow batteries.* Journal of Applied Electrochemistry, 2018. **48**(9): p. 1043-1056.

View Article Online
DOI: 10.1039/D5TA07792C

20. Trudgeon, D.P., et al., *Screening of effective electrolyte additives for zinc-based redox flow battery systems.* Journal of Power Sources, 2019. **412**: p. 44-54.
21. Kellamis, C.J. and J.S. Wainright, *A zinc–iodine hybrid flow battery with enhanced energy storage capacity.* Journal of Power Sources, 2024. **589**: p. 233753.
22. Xu, Z., et al., *Review of zinc dendrite formation in zinc bromine redox flow battery.* Renewable and Sustainable Energy Reviews, 2020. **127**: p. 109838.
23. Bockelmann, M., U. Kunz, and T. Turek, *Electrically rechargeable zinc-oxygen flow battery with high power density.* Electrochemistry Communications, 2016. **69**: p. 24-27.
24. Richtr, P., et al., *Nickel-cobalt spinel-based oxygen evolution electrode for zinc-air flow battery.* Journal of Energy Storage, 2025. **115**: p. 115835.
25. Zhao, Y., et al., *Accelerating the dissolution kinetics of iodine with a cosolvent for a high-current zinc–iodine flow battery.* Journal of Materials Chemistry A, 2022. **10**(26): p. 14090-14097.
26. Vrána, J., et al., *Commercial perfluorosulfonic acid membranes for vanadium redox flow battery: Effect of ion-exchange capacity and membrane internal structure.* Journal of Membrane Science, 2018. **552**: p. 202-212.
27. Gubler, L., *Membranes and separators for redox flow batteries.* Current Opinion in Electrochemistry, 2019. **18**: p. 31-36.
28. Charvát, J., et al., *The role of ion exchange membrane in vanadium oxygen fuel cell.* Journal of Membrane Science, 2021. **629**: p. 119271.
29. Xie, C., et al., *A Long Cycle Life, Self-Healing Zinc–Iodine Flow Battery with High Power Density.* Angewandte Chemie International Edition, 2018. **57**(35): p. 11171-11176.
30. Xie, C., et al., *Highly stable zinc–iodine single flow batteries with super high energy density for stationary energy storage.* Energy & Environmental Science, 2019. **12**(6): p. 1834-1839.
31. Weng, G.-M., et al., *Unlocking the capacity of iodide for high-energy-density zinc/polyiodide and lithium/polyiodide redox flow batteries.* Energy & Environmental Science, 2017. **10**(3): p. 735-741.
32. Mazúr, P., et al., *Performance evaluation of thermally treated graphite felt electrodes for vanadium redox flow battery and their four-point single cell characterization.* Journal of Power Sources, 2018. **380**: p. 105-114.
33. Savsatli, Y., et al., *In Situ and Operando Observation of Zinc Moss Growth and Dissolution in Alkaline Electrolyte for Zinc–Air Batteries.* ACS Energy Letters, 2024. **9**(7): p. 3516-3525.
34. Mousavi, M., et al., *Decoupled low-cost ammonium-based electrolyte design for highly stable zinc–iodine redox flow batteries.* Energy Storage Materials, 2020. **32**: p. 465-476.
35. Charvát, J., et al., *Performance enhancement of vanadium redox flow battery by optimized electrode compression and operational conditions.* Journal of Energy Storage, 2020. **30**: p. 101468.
36. Bureš, M., et al., *Mathematical modeling of electric and hydraulic resistances of reconstructed carbon felt electrodes using micro-computed tomography.* Chemical Engineering Journal, 2023. **458**: p. 141424.
37. Bureš, M., et al., *Evaluation of mitigation of capacity decay in vanadium redox flow batteries for cation- and anion-exchange membrane by validated mathematical modelling.* Journal of Power Sources, 2024. **591**: p. 233769.

View Article Online
DOI: 10.1039/D5TA07792C

38. Jian, Q.P., et al., *A trifunctional electrolyte for high-performance zinc-iodine flow batteries*. Journal of Power Sources, 2021. **484**: p. 229238.
39. Li, Y., et al., *Homogenizing Zn Deposition in Hierarchical Nanoporous Cu for a High-Current, High Areal-Capacity Zn Flow Battery*. Small, 2023. **19**(40): p. 2303005.

Data for this article are available at Zenodo at 10.5281/zenodo.17175636. This DOI represents all versions and will always resolve to the latest one.

View Article Online
DOI: 10.1039/D5TA07792C